Electro–Thermal Vertical-Cavity Surface-Emitting Laser Simulation

Markus Daubenschuez

For ongoing optimization of GaAs-based vertical-cavity surface-emitting lasers (VCSELs) it is necessary to predict the current flow and the heat generation of new epitaxial and geometrical designs. To implement a VCSEL model it turned out to be necessary to revisit basic material parameters like the composition, carrier density, and temperature dependencies of the electron and hole mobilities of $Al_xGa_{1-x}As$ semiconductors. In this article we present our quasi-three-dimensional (q3D) electro–thermal device modeling approach and compare the simulation results with current–voltage and wavelength shift measurements.

1. Introduction

VCSELs are established in many technical fields today, in particular optical data communication and sensing [1]. New applications of high-power sources for thermal material treatment or illumination systems are at the horizon. For continuous optimization it is important to have a reliable prediction of the electro–thermal characteristics of such devices and arrays. Several approaches have already been presented in the literature [2–4]. The main difficulty in electrical modeling is the multitude of heterojunctions in the distributed Bragg reflectors (DBRs). It is an extremely demanding task for every commercial semiconductor device simulator to compute the q3D current density distributions and energy band alignments in a full VCSEL. Simplifications are thus necessary.

In Sect. 2 we introduce simple but well suited expressions for the electron and hole mobilities in $Al_xGa_{1-x}As$. We describe the basic scattering mechanisms that limit the mobility of carriers and show comparisons between our model and values given in literature. In Sect. 3 we present the electro–thermal VCSEL simulator, able to handle q3D geometries. We process the whole longitudinal layer structure of a VCSEL with the public domain software SimWindows that gives, among others, spatially resolved carrier density profiles as well as the current–voltage (IV) characteristic. In a further step we combine the data to get a linearized q3D model of the VCSEL itself. The current density distribution inside the entire structure is calculated from the potential profile that is obtained by solving the electrostatic Laplace equation. We then can find the dissipated power density distribution and get the internal temperature profile of the VCSEL. From the calculated temperature profiles we predict the resonance wavelength shifts of the VCSELs which are easily accessible parameters. We show simulation results of VCSEL structures and make comparisons with experimental data.

2. Carrier Mobility

For the simulation of electronic devices, the carrier mobility in the compound semiconductors is one of the key parameters [4]. In the past, quite some effort was put in performing Hall effect measurements [5–8] and provide theoretical descriptions [9] of the carrier mobility. Most of these measurements are in a temperature range irrelevant for practical device applications (typically 77 K) and the theoretical formulations are too complex to use them in a simulation environment. In what follows we describe the most important scattering mechanisms for $Al_xGa_{1-x}As$ and show a combined analytic description of the electron mobility depending on the input parameters temperature, carrier density, and material composition. We show the validity of the formula by comparing the calculated mobilities with experimental data from the literature.

2.1 Scattering mechanisms

The mobility of carriers in a bulk material is defined as

$$\mu = \frac{q}{m_{\text{eff}}} \tau_{\text{sc}} \,, \tag{1}$$

where q is the elementary charge, m_{eff} is the effective mass, and τ_{sc} is the average scattering time. Different scattering effects reduce τ_{sc} and therefore limit the mobility of carriers. The main effects described by Stringfellow [10] are polar optical mode scattering, piezoelectrical scattering, deformation potential scattering, ionized impurity-limited scattering, and space-charge scattering. For electro–thermal simulation we are especially interested in the temperature dependence of the mobility. In the case of ionized impurity-limited scattering we have a relation between the mobility μ_{ii} and the temperature T of the form

$$\mu_{\text{ii}} \propto T^{3/2} \,, \tag{2}$$

causing an increase of μ_{ii} with T due to higher kinetic energy of the carriers. In contrast, all other scattering mechanisms reduce the electron mobility. For instance, the mobility μ_{dp} arising from deformation potential scattering has a proportionality

$$\mu_{\text{dp}} \propto T^{-3/2} \,. \tag{3}$$

This kind of scattering is induced by acoustic phonons which have a larger oscillation for higher temperature. The total scattering in a semiconductor is the sum of all contributions. Thus one can calculate the total mobility μ_{tot} as the reciprocal sum

$$\frac{1}{\mu_{\text{tot}}} = \sum_i \frac{1}{\mu_i} \tag{4}$$

over all individual mobilities μ_i. Figure 1 shows a characteristic mobility curve $\mu_{\text{tot}}(T)$ with contributions of scattering at ionized impurities and deformation potential scattering. These two mechanisms lead to a maximum mobility for a certain temperature.

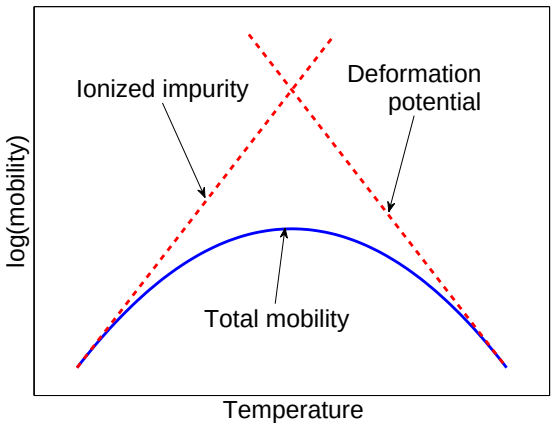

Fig. 1: Total mobility as a function of temperature with two main scattering mechanisms in a semi-logarithmic plot (schematic).

2.2 Electron mobility

To provide a full quantitative model for the electron mobility, one needs to know many material constants like the deformation potentials. One may find these parameters for binary compounds, however, they are hardly available for ternaries. Furthermore one has to describe each scattering mechanism individually. Sotoodeh et al. [11] have developed a low-field Caughey–Thomas-like mobility model for III–V compounds. The model is based on empirical parameters of binary compounds and uses physically justifiable linear interpolations for ternary materials. For our purpose it is convenient to have a single analytical expression for the electron mobility depending on the temperature, the alloy composition, and the carrier density. It should be applicable for practical parameter ranges like temperatures T from 200 to 500 K and electron densities n from $1 \cdot 10^{15}$ to $5 \cdot 10^{18}\,\mathrm{cm}^{-3}$. Therefore we made some simplifications in the parameter set of Sotoodeh's formula which has the form

$$\mu_\mathrm{n}(x,n,T) = \mu_\mathrm{n,min}(x) + \frac{\mu_{\mathrm{n},x} \cdot (300\,\mathrm{K}/T)^{\zeta_\mathrm{n1}(x)} - \mu_\mathrm{n,min}(x)}{1 + \left(\frac{n}{n_\mathrm{ref}(x)\cdot(T/(300\,\mathrm{K}))^{\zeta_\mathrm{n2}}}\right)^{\zeta_\mathrm{n3}(x)}} \tag{5}$$

with the alloy-dependent mobility $\mu_{\mathrm{n},x}$ and the saturated mobility $\mu_\mathrm{n,min}$ for very high n. The electron density at which the mobility reduces to almost half of its maximum value for low doping at a temperature of 300 K is given by n_ref. In contrast to $\mu_\mathrm{n,min}$, $\mu_{\mathrm{n},x}$ and n_ref are temperature-dependent, which is considered by the terms $(300\,\mathrm{K}/T)^{\zeta_\mathrm{n1}}$ and $(T/\,(300\,\mathrm{K}))^{\zeta_\mathrm{n2}}$. The exponent $\zeta_\mathrm{n2} = 3$ is constant for AlGaAs. All parameters in (5) are listed in Table 1. The dependence of n_ref on the alloy concentration is approximated by [11]

$$n_\mathrm{ref}(x) = (n_\mathrm{ref}\,(x=0))^{1-x} \cdot (n_\mathrm{ref}\,(x=1))^{x} \quad . \tag{6}$$

The value of ζ_n1 for different compositions of $\mathrm{Al}_x\mathrm{Ga}_{1-x}\mathrm{As}$ is [11]

$$\zeta_\mathrm{n1}(x) = \frac{(1-x)\zeta_\mathrm{n1}(x=0) + x\zeta_\mathrm{n1}(x=1)}{1+x(1-x)} = \frac{2.1}{1+x(1-x)} \tag{7}$$

Table 1: Fit parameters for the low-field electron mobility after Sotoodeh [11].

Material	$\mu_{\mathrm{n,min}}$ ($\mathrm{cm}^2/(\mathrm{Vs})$)	n_{ref} at 300 K (cm^{-3})	ζ_{n1}	ζ_{n2}	ζ_{n3}
GaAs	500	$6.00 \cdot 10^{16}$	2.1	3	0.394
AlAs	10	$5.46 \cdot 10^{17}$	2.1	3	1.00

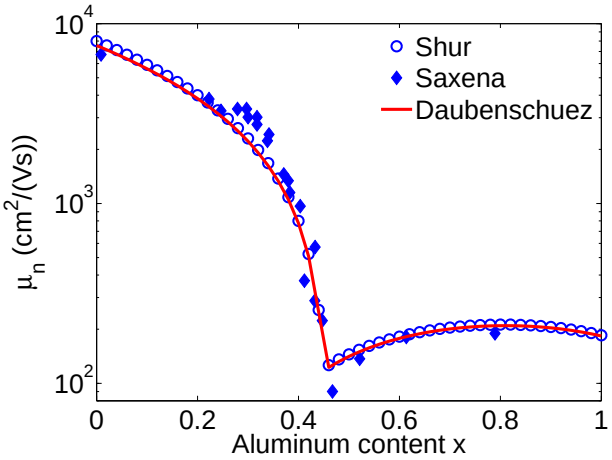

Fig. 2: Electron mobility at $T = 300\,\mathrm{K}$ depending on the fraction x of $\mathrm{Al}_x\mathrm{Ga}_{1-x}\mathrm{As}$ for a free electron density of $n = 5 \cdot 10^{15}\,\mathrm{cm}^{-3}$. Calculated values are compared with Saxena [6] and Shur [12].

according to Table 1. $\zeta_{\mathrm{n3}}(x)$ is linearly interpolated between the values for GaAs and AlAs. The difference between our model and that of Sotoodeh lies in the values for $\mu_{\mathrm{n},x}$ and $\mu_{\mathrm{n,min}}$. To get the typical drop of mobility for $x \approx 45\,\%$ we use the model after Shur [12] as input for $\mu_{\mathrm{n},x}$. In this case, the alloy composition is split into ranges with $x < 0.45$ and $x \geq 0.45$ and $\mu_{\mathrm{n},x}$ is described by the polynomial equations

$$\frac{\mu_{\mathrm{n},x}}{\mathrm{cm}^2/\,(\mathrm{Vs})} = \begin{cases} 8000 - 22000x + 10000x^2 & \text{for } 0 \leq x < 0.45\,, \\ -255 + 1160x - 720x^2 & \text{for } 0.45 \leq x \leq 1\,. \end{cases} \tag{8}$$

To maintain this mobility drop we decided to change also the linearization of $\mu_{\mathrm{n,min}}$ recommended by Sotoodeh. With a simple linear interpolation between $\mu_{\mathrm{n,min}}(x = 0)$ and $\mu_{\mathrm{n,min}}(x = 1)$ we would overestimate the mobility in the low-mobility range around $x = 45\,\%$. Therefore we choose a small value $\mu_{\mathrm{n,min}}(x = 0.45) = 1$ and linearly interpolate between $\mu_{\mathrm{n,min}}(x = 0)$ and $\mu_{\mathrm{n,min}}(x = 0.45)$ or between $\mu_{\mathrm{n,min}}(x = 0.45)$ and $\mu_{\mathrm{n,min}}(x = 1)$. The calculated room-temperature electron mobilities depending on the alloy composition in Fig. 2 show a good agreement with the experimental data [6] and are nearly congruent with the temperature-independent model by Shur [12]. The results for the temperature and carrier density dependences are shown in Fig. 3. All calculated results are in the uncertainty range of the measurement data found in literature.

However, it should be mentioned that the model has the same limitations as described by Sotoodeh [11]. Additionally our model is limited to a lowest temperature in the range of

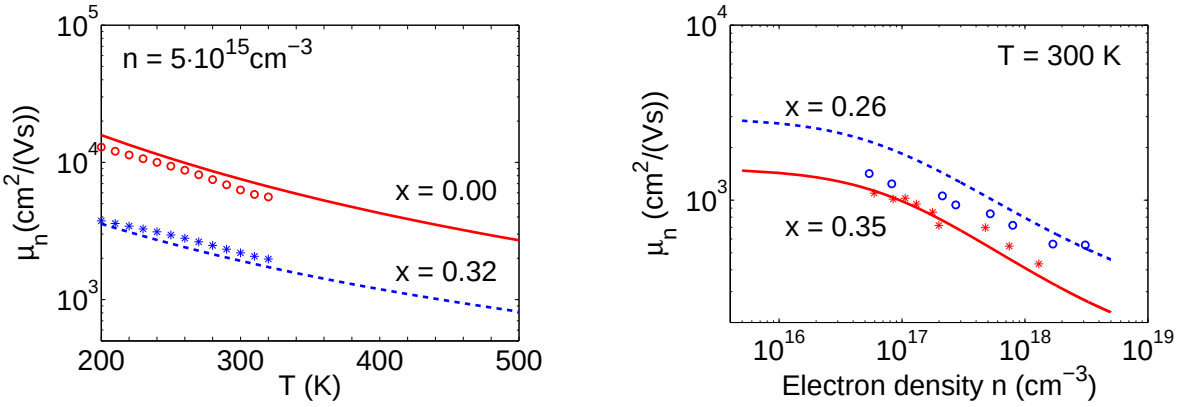

Fig. 3: Calculated (full and dashed lines) electron mobility depending on temperature T (left) and electron density n (right) as well as experimental data (symbols): $x = 0.00$ [7], $x = 0.26$ [8], $x = 0.32$ [6], $x = 0.35$ [8].

200 K. Due to the simplifications made, we do not need to take ionized impurity-limited scattering into account.

2.3 Hole mobility

Like the electron mobility model from the previous section, the model for the hole mobility μ_p is also based on Sotoodeh [11], namely

$$\mu_\mathrm{p}(x,p,T) = \mu_\mathrm{p,min}(x) + \frac{\mu_{\mathrm{p},x}\cdot(300\,\mathrm{K}/T)^{\zeta_\mathrm{p1}(x)} - \mu_\mathrm{p,min}(x)}{1+\left(\frac{p}{p_\mathrm{ref}(x)\cdot(T/(300\,\mathrm{K}))^{\zeta_\mathrm{p2}}}\right)^{\zeta_\mathrm{p3}(x)}} \tag{9}$$

with the alloy-dependent mobility $\mu_{\mathrm{p},x}$ and the saturated hole mobility $\mu_\mathrm{p,min}$ for high hole densities p. All parameters in (9) are listed in Table 2. For computing $\mu_{\mathrm{p},x}$ we use the alloy dependence

$$\mu_{\mathrm{p},x} = 370 - 970x + 740x^2 \tag{10}$$

after Shur [12]. To calculate the saturated mobility, the alloy composition is split into ranges with $x < 0.3$ and $x \geq 0.3$ and therefore $\mu_\mathrm{p,min}$ is described by the linearizations

$$\frac{\mu_\mathrm{p,min}}{\mathrm{cm}^2/(\mathrm{Vs})} = \begin{cases} 20 - 50x & \text{for } 0 \leq x < 0.3\,, \\ 2.857 + 7.142x & \text{for } 0.3 \leq x \leq 1\,. \end{cases} \tag{11}$$

The meaning of p_ref is equivalent to that of n_ref in (5). The values for p_ref and ζ_p3 are calculated with a quadratic interpolation between the data given in Table 2:

$$p_\mathrm{ref}(x) = \left(1.48 - 3.297\cdot x + 5.657\cdot x^2\right)\cdot 10^{17}\,\mathrm{cm}^{-3}\,, \tag{12}$$

$$\zeta_\mathrm{p3}(x) = 0.38 - 0.313\cdot x + 0.421\cdot x^2\,. \tag{13}$$

For ζ_p1 a simple linearized relation

$$\zeta_\mathrm{p1}(x) = 2.2 + 0.04\cdot x \tag{14}$$

Table 2: Fit parameters for the low-field hole mobility after Sotoodeh [11].

Material	$\mu_{\mathrm{p,min}}$ ($\mathrm{cm}^2/(\mathrm{Vs})$)	p_{ref} at 300 K (cm^{-3})	ζ_{p1}	ζ_{p2}	ζ_{p3}
GaAs	20	$1.48 \cdot 10^{17}$	2.2	3	0.38
$Al_{0.3}Ga_{0.7}As$	5	$1 \cdot 10^{17}$			0.324
AlAs	10	$3.84 \cdot 10^{17}$	2.24	3	0.488

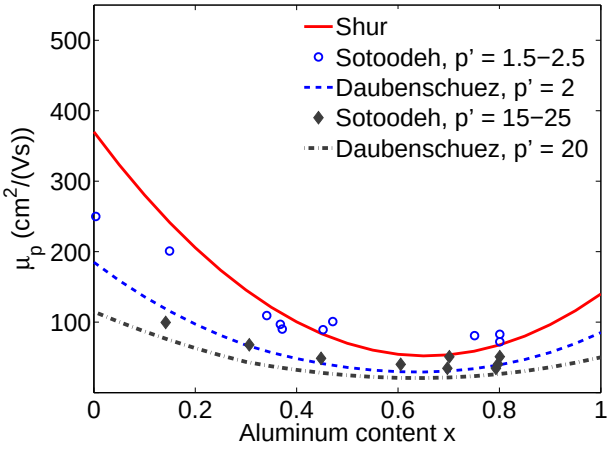

Fig. 4: Hole mobility μ_{p} for different fractions x of $Al_xGa_{1-x}As$ and free hole densities $p = p' \cdot 10^{17}\,\mathrm{cm}^{-3}$ at room temperature. Calculated values are compared with Shur [12] and Sotoodeh [11].

is used. $\zeta_{\mathrm{p2}} = 3$ is assumed for all x. Simulation results for the alloy-dependent mobilities at room temperature are shown in Fig. 4 for different hole densities. The results are compared with measurement data from [11]. Figure 5 shows results for the temperature (left) and carrier density dependence (right). The computed curves are compared with measured data from [13] and [8]. The results are in the uncertainty range of literature data.

3. VCSEL Model

High-power VCSELs are beginning to enable new applications [14, 15]. In parallel there is ongoing research in the more traditional fields of optical data communication and sensing [1]. For continuous optimization it is important to have a reliable prediction of the electro–thermal characteristics of such devices and arrays. In optical data communication, as an example, the constant increase in bandwidth demand requires higher modulation frequencies of the lasers. Neglecting device heating, the resonance frequency ν_{r} can be increased with the injected current I above the threshold current I_{th} according to [16]

$$\nu_{\mathrm{r}} \propto \sqrt{I - I_{\mathrm{th}}}\ .$$

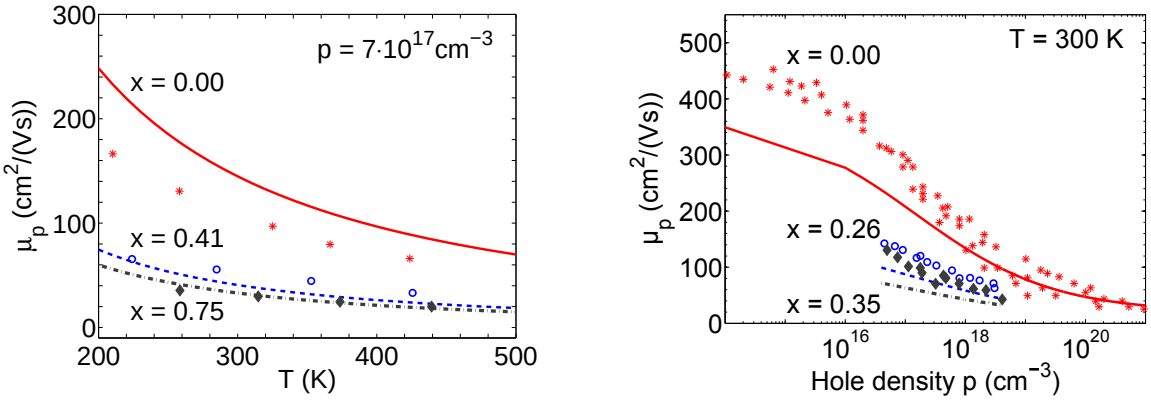

Fig. 5: Calculated (full and dashed lines) hole mobility μ_p depending on temperature T (left) and hole density p (right) as well as experimental data (symbols) from [13] (left) and [8] (right).

In practice, ν_r is limited by thermal effects due to electrical losses in the laser. The motivation behind the simulation model discussed in this paper is the prediction of the electro–thermal behavior of VCSELs and finally the reduction of the dissipated power. In the following we describe the simulation environment that is based on the software SimWindows and a solution of the electrostatic Laplace equation

$$\nabla \cdot \nabla V = 0 \tag{15}$$

with the nabla operator ∇ and the electric potential V as well as of the heat conduction equation

$$\nabla \cdot (\lambda_\mathrm{c} \nabla T) = -p_\mathrm{diss} \tag{16}$$

with the thermal conductivity λ_c and the dissipated power density p_diss.

3.1 Simulation process

All input parameters for the simulation except for the transverse dimensions (active, mesa, and contact diameters) of the oxide-confined VCSELs are given by an epitaxial design file. For each epitaxial layer this file includes the thickness, the alloy gradient, the doping gradient, and the doping material. These parameters are extracted and written into a SimWindows structure definition file.

The 1D energy band alignment is then calculated for the whole structure with the software SimWindows [17], which is a semiconductor device simulation tool that works by solving the semiconductor equations in one dimension. The software thus assumes that all variables such as electron current density j_n, hole current density j_p, electric potential, etc. vary parallel to the flow direction of the current but are uniform in the perpendicular direction. Current continuity $j_\mathrm{n} + j_\mathrm{p} = \mathrm{const}$ is fulfilled. To handle heterojunctions it has a built-in model based on thermionic emission and tunneling currents. To include the temperature dependencies, we have extended the material database of SimWindows by the electron and hole mobility models introduced in Sect. 2. The energy band calculation is done for different material temperatures and voltages between the contacts. Thus we

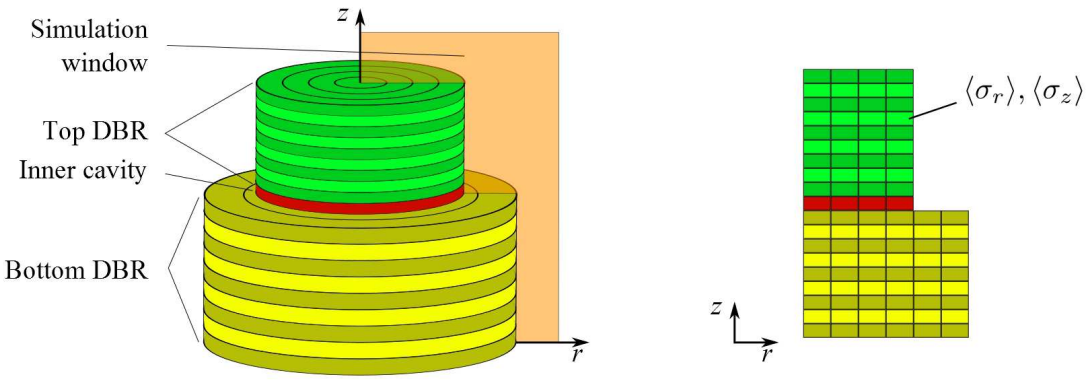

Fig. 6: Calculation plane for the VCSEL simulation (left) and discretization mesh (right).

derive a temperature-dependent longitudinal 1D current–voltage (IV) characteristic of the whole structure. From such an IV characteristic we can derive an average conductivity $\langle\sigma_z\rangle$ for each discretization step in longitudinal z-direction by taking the current density through the whole structure and the voltage drop over each discretization element into account. SimWindows also provides the local carrier densities and mobilities on a user-defined grid with, e.g., 1 nm step width. From those data we calculate a local conductivity $\sigma(z) = q\,(n(z)\cdot\mu_\mathrm{n}(z) + p(z)\cdot\mu_\mathrm{p}(z))$. For in-plane current transport that is not impeded by heterojunctions, we transform the various $\sigma(z)$ into an average conductivity $\langle\sigma_r\rangle$ of the actual discretization block according to a parallel circuit of ohmic resistors.

From the derived data $\langle\sigma_z\rangle$ and $\langle\sigma_r\rangle$ we build a q3D model of the VCSEL. We exploit rotational symmetry and consider only an $(r,\,z)$-plane, as shown in Fig. 6. The plane is divided into segments in lateral r- and vertical z-direction with the discretization widths Δr and Δz.

Once the model of the VCSEL is established, we start the calculation by applying a voltage between the contacts. The following steps are taken iteratively:

1. Solve (15) equivalent to the approach described in [18] to get the potential distribution $V(r, z)$ inside the device.
2. Get the current density and dissipated power density profiles using $\langle\sigma_r\rangle$ and $\langle\sigma_z\rangle$.
3. Take photon cooling in the quantum wells into account.
4. Solve (16) with a fixed heat sink temperature to find $T(r, z)$.
5. Adapt the electric and thermal conductivity values using $T(r, z)$ from step 4.

Those five steps are iterated for each voltage until the total current I converges.

3.2 Simulation results

We now present some results obtained with the described model. Figure 7 shows the electric potential and temperature profiles of a VCSEL with 6.5 µm active diameter. A voltage of 2 V is applied to the top ring contact of the VCSEL at $z = 0\,\mu\text{m}$. The epitaxial layer stack and the substrate have thicknesses of 8.86 µm and 120 µm, respectively. The top mesa diameter is approximately 27.5 µm and the n-DBR region has a diameter of 100 µm. The figures show only the inner part of the VCSEL. The n-contact of the laser is at the back side of the substrate at $z = 128.86\,\mu\text{m}$. Outside the semiconductor material, the electric conductivity is zero and the potential is set to an arbitrary value of −1 V. The top mesa is surrounded by polyimide with a thermal conductivity $\lambda_c = 0.445\,\text{W}/(\text{m}\cdot\text{K})$. As intended, the oxide aperture is strictly blocking the current flow that is perpendicular to the equipotential lines. The main voltage drop obviously occurs over the pn-junction of the active region. The right graph displays the temperature profile for a dissipated power of $P_{\text{diss}} = 9.6\,\text{mW}$. The heat sink is on the back side of the substrate and has a constant temperature of 300 K. No heat flow is assumed across all other surfaces. The maximum temperature increase is $\Delta T_{\text{max}} = 26.14\,\text{K}$ close to the oxide aperture. The corresponding non-averaged thermal resistance of this device thus amounts to $\Delta T_{\text{max}}/P_{\text{diss}} = 2.72\,\text{K/mW}$.

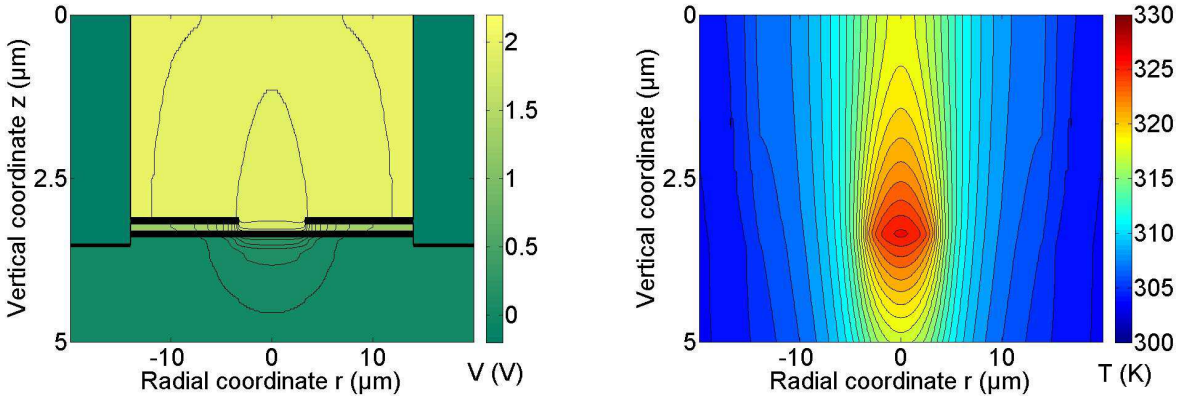

Fig. 7: Simulated electric potential profile $V(r, z)$ (left) and temperature profile $T(r, z)$ (right) of a VCSEL test structure. The oxide aperture is located at $z \approx 3.12\,\mu\text{m}$.

To check the validity of the electro–thermal model we compare it with experimental data of 850 nm GaAs-based VCSELs grown and fabricated by Philips (U-L-M Photonics). First we determine the IV curves of the VCSEL structure described above with two different active diameters D_a. The experimental data in Fig. 8 show excellent agreement with the simulations. A current density distribution $j_z(r, z)$ is also depicted for illustration. The results are obtained without adjustable parameters. We confirm the validity of the approach also via a comparison of the emission wavelength shift as a function of the dissipated power in Fig. 9 for different ambient temperatures T_a. Here, the temperature profile that acts on the refractive indices is weighted by the resonant mode pattern with optical transfer matrix calculations.

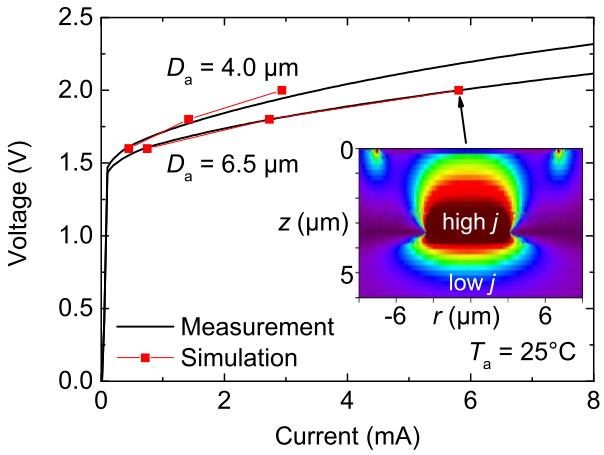

Fig. 8: Simulated and measured IV characteristics for $T_\mathrm{a} = 25°\mathrm{C}$ heat sink temperature and two different active diameters D_a. The inset shows the longitudinal current density distribution $j = j_z$ for $V = 2\,\mathrm{V}$, $D_\mathrm{a} = 6.5\,\mu\mathrm{m}$, and $T_\mathrm{a} = 25°\mathrm{C}$.

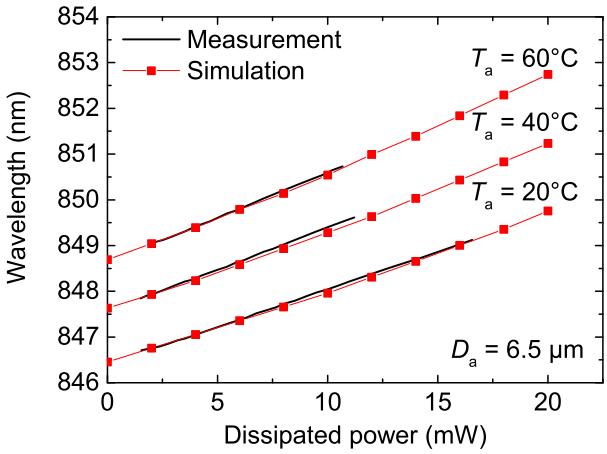

Fig. 9: Dissipated-power-dependent thermal wavelength shifts of a VCSEL with $D_\mathrm{a} = 6.5\,\mu\mathrm{m}$ for various T_a.

4. Conclusion

In this article we have introduced a pragmatic approach to q3D electro–thermal VCSEL simulations employing a proven 1D semiconductor solver. The strong variations of the electron and hole mobilities with composition, temperature, and electron density required to extend the material database of SimWindows with a modified mobility model. The electrical and thermal simulations correspond very well to experimental data. In future we will extend the simulation tool with a simple optical model to take photon cooling and absorption more accurately into account.

Acknowledgment

We would like to thank Dr.-Ing. Philipp Gerlach and Dipl.-Ing. Roger King from Philips Technologie GmbH (U-L-M Photonics) for fruitful discussions and the provision of VCSEL samples. We are grateful to the German Federal Ministry of Education and Research (BMBF) for funding the HyPOT project.

References

[1] R. Michalzik (Ed.), *VCSELs — Fundamentals, Technology and Applications of Vertical-Cavity Surface-Emitting Lasers*. Berlin: Springer, 2013.

[2] S.F. Yu, *Analysis and Design of Vertical Cavity Surface Emitting Lasers*. Hoboken: John Wiley & Sons, 2003.

[3] P. Debernardi, "Three-Dimensional Modeling of VCSELs", Chap. 3 in *VCSELs*, R. Michalzik (Ed.), pp. 77–117. Berlin: Springer, 2013.

[4] J. Piprek, *Semiconductor Optoelectronic Devices*. San Diego: Academic Press, 2003.

[5] S. Adachi, *Properties of Aluminium Gallium Arsenide*. London: INSPEC, 1993.

[6] A.K. Saxena, "Electron mobility in $Ga_{1-x}Al_xAs$", *Phys. Rev. B*, vol. 24, pp. 3295–3302, 1981.

[7] G. Stillman, C. Wolfe, and J. Dimmock, "Hall coefficient factor for polar mode scattering in n-type GaAs", *J. Phys. Chem. Solids*, vol. 31, pp. 1199–1204, 1970.

[8] W.C. Liu, "Investigation of electrical and photoluminescent properties of MBE-grown $Al_xGa_{1-x}As$ layers", *J. Material Sci.*, vol. 25, pp. 1765–1772, 1990.

[9] H.S. Bennett, "Majority and minority electron and hole mobilities in heavily doped gallium aluminium arsenide", *J. Appl. Phys.*, vol. 80, pp. 3844–3853, 1996.

[10] G. Stringfellow, "Electron mobility in $Al_xGa_{1-x}As$", *J. Appl. Phys.*, vol. 50, pp. 4178–4183, 1979.

[11] M. Sotoodeh, A.H. Khalidan, and A.A. Rezazadeh, "Empirical low-field mobility model for III-V compounds applicable in device simulation codes", *J. Appl. Phys.*, vol. 87, pp. 2890–2900, 1999.

[12] M. Shur, *Physics of Semiconductor Devices*. Englewood Cliffs: Prentice Hall, 1990.

[13] J.J. Yang, W.I. Simpson, and L.A. Moudy, "Hole Hall mobility versus temperature". Web page: http://www.ioffe.ru/SVA/NSM/Semicond/AlGaAs/hall.html; last visited Feb. 2015.

[14] J.F.P. Seurin, "High-Power VCSEL Arrays", Chap. 8 in *VCSELs*, R. Michalzik (Ed.), pp. 263–290. Berlin: Springer, 2013.

[15] H. Moench, R. Dumoulin, S. Gronenborn, X. Gu, G. Heusler, J. Kolb, M. Miller, P. Pekarski, J. Pollmann-Retsch, A. Pruijmboom, and M. Stroesser, "Design of high power VCSEL arrays", in *Vertical-Cavity Surface-Emitting Lasers XVI*, C. Lei and K.D. Choquette (Eds.), Proc. SPIE, vol. 8276, pp. 82760B-1–8, 2012.

[16] R. Michalzik, "VCSEL Fundamentals", Chap. 2 in *VCSELs*, R. Michalzik (Ed.), pp. 19–75. Berlin: Springer, 2013.

[17] D.W. Winston, *Physical Simulation of Optoelectronic Semiconductor Devices*. Ph.D. Thesis, University of Colorado, Boulder, CO, USA, 1990.

[18] P. Gerlach, M. Peschke, C. Hanke, B.K. Saravanan, and R. Michalzik, "High-frequency analysis of laser-integrated lumped electroabsorption modulators", *IEE Proc.-Optoelectron.*, vol. 152, pp. 125–130, 2005.